

## IMAGING A QUASAR ACCRETION DISK WITH MICROLENSING

ERIC AGOL AND JULIAN KROLIK

Physics and Astronomy Department, Johns Hopkins University, Baltimore, MD 21218

*Draft version April 29, 2024*

### ABSTRACT

We show how analysis of a quasar high-magnification microlensing event may be used to construct a map of the frequency-dependent surface brightness of the quasar accretion disk. The same procedure also allows determination of the disk inclination angle, the black hole mass (modulo the caustic velocity), and possibly the black hole spin. This method depends on the validity of one assumption: that the optical and ultraviolet continuum of the quasar is produced on the surface of an azimuthally symmetric, flat equatorial disk, whose gas follows prograde circular orbits in a Kerr spacetime (and plunges inside the marginally stable orbit). Given this assumption, we advocate using a variant of first-order linear regularization to invert multi-frequency microlensing lightcurves to obtain the disk surface brightness as a function of radius and frequency. The other parameters can be found by minimizing  $\chi^2$  in a fashion consistent with the regularized solution for the surface brightness.

We present simulations for a disk model appropriate to the Einstein Cross quasar, an object uniquely well-suited to this approach. These simulations confirm that the surface brightness can be reconstructed quite well near its peak, and that there are no systematic errors in determining the other model parameters. We also discuss the observational requirements for successful implementation of this technique.

*Subject headings:* accretion, accretion disks — gravitational lensing — quasars: individual (2237+0305)  
— relativity

### 1. INTRODUCTION

Due to their great distance and small intrinsic size, it is not possible to obtain a resolved optical image of a quasar with current technology. The angular size of a quasar optical emission region is of order  $10^{-8}''$ , a scale so small as to require a baseline of several thousand kilometers to resolve. Thus, until optical VLBI becomes practical, quasar structure will need to be probed by other, indirect, means. Reverberation mapping provides an instructive example of the difficulties of such indirect approaches, for it has proven difficult both to implement and to interpret. We believe that the subject of this paper, microlensing by stars in an intervening galaxy, is a more promising method.

The circumstantial evidence that black holes power quasars is convincing: accretion onto black holes can be very efficient in converting rest mass energy to photons (up to 40%) or to bulk momentum (forming radio jets/lobes) in a compact region which has an effective temperature near where the quasar spectrum peaks. There is statistical evidence that quiescent black holes in the nuclei of galaxies at low redshift could be the remnants of quasars. And, quasars have properties very similar to Seyfert galaxies, for some of which there is good spectroscopic evidence for a central black hole. The nature of the accretion flow is quite uncertain, however, although it is probably geometrically thin since angular momentum will support the accretion flow against collapse and geometrically thick disks are by nature inefficient (if quasar disks were thick, there would be problems producing the huge luminosities observed within a reasonable mass budget).

Attempts to constrain the character of the innermost accretion flow by means of spectral modeling have made little progress for several reasons. There are major systematic uncertainties about fundamental issues (e.g., the

vertical distribution of energy dissipation, the physics to include in radiation transfer solutions). In addition, any particular model depends on a sizable number of free parameters (mass of the central black hole, accretion rate, viscosity parameter, inclination angle), so that parameter estimation is tricky.

Analysis of a microlensing event is potentially a more powerful tool. Rather than guess a specific model for the accretion disk, the history of magnification in the event can be used to directly infer the disk surface brightness as a function of radius and frequency. The only assumptions required are that the continuum emission surface is geometrically flat, the material forming it follows circular orbits, and general relativity determines the dynamics of both the matter and the photons.

To apply this technique requires study of a particular gravitationally-lensed quasar. Many are now known, and some appear to undergo occasional fluctuations due to individual stars in the lens galaxy magnifying the quasar, a phenomenon referred to as microlensing. The Einstein Cross is particularly well-suited to this problem for a number of reasons that we will detail in §1.3. Several authors have attempted to constrain the character of the accretion disk in this system by comparing predicted lightcurves to the data compiled during microlensing events (Jaroszyński et al. 1992, Rauch & Blandford 1991, Jaroszyński & Marck 1994, Czerny et al. 1994). However, the results have all been somewhat inconclusive due to the ordinary spectral modeling difficulties described above.

The remainder of this paper is organized as follows: In §1, we describe how a caustic crossing can be used to perform the mapping, and discuss why the Einstein Cross is such a suitable target for this sort of study. In §2, we discuss the model in detail, considering our assumptions,

the inversion technique, and error propagation. In §3, we present a variety of simulations of caustic-crossing events, and demonstrate that we can measure most model parameters. We show some examples of the accuracy with which the intensity at the accretion disk may be determined, and discuss how the reliability of the results depends on the quality of the observational data, on the character of the monitoring, and, to some degree, on the character of the regularization scheme. In the final section, we discuss the results and present our conclusions.

### 1.1. Smooth thin disk

For a standard thin accretion disk with constant accretion rate and no advection of heat, the energy generation per unit area as a function of radius is given by

$$Q = \frac{3}{4\pi} \frac{GM_{BH}\dot{M}}{r^3} R_R(r). \quad (1)$$

where  $M_{BH}$  is the mass of the black hole,  $\dot{M}$  is the accretion rate,  $r$  is the radius within the disk, and  $R_R$  is a correction factor that combines outward advection of energy associated with the angular momentum flux and relativistic effects (Page & Thorne 1974, notation from Krolik 1998).  $R_R$  is a function of the black hole spin  $a_s = a/M_{BH}$ .

Though equation [1] describes the functional dependence of the energy released with radius, it does not specify whether this energy is thermal or mechanical, and does not specify the dissipation as a function of height within the accretion disk. The appearance of a standard thin accretion disk can vary significantly depending on how and where the energy is released. To further our understanding, it would be very desirable to actually measure the local spectrum.

One potential method to achieve this is to observe a quasar during the sort of high-magnification microlensing event that occurs when a caustic crosses the source (Grieger et al., 1988 and 1991, Gould & Gaudi 1997). Grieger et al. (1991) advocate inverting the microlensing lightcurve to obtain the one-dimensional surface brightness of the quasar,  $P_\nu(x) = \int I_\nu(x, y) dy$ , where  $I_\nu(x, y)$  is the specific intensity of the quasar at sky coordinates  $(x, y)$ . Their method is quite elegant, but relies on first-order regularization (the assumption that the quasar profile is smooth). This assumption is problematic for black hole models since the energy release increases rapidly towards smaller radii, and relativistic effects can cause sharp peaks in the quasar profile. These sharp features are smoothed out when this method is used (see Figure 1).

We believe a better approach is to solve instead for the surface brightness at the accretion disk, with the relatively benign assumptions that the disk is planar, axisymmetric, and isotropically emitting (in the fluid frame), and most importantly, likely to vary smoothly with radius. This approach provides a better inversion of the quasar profile if the disk assumptions are correct. This method recovers the spectrum as a function of radius at the accretion disk, which can then be compared with disk atmosphere models or other spectral modeling. In addition, it can help constrain disk parameters, such as the inclination angle, without relying on a specific accretion disk spectral model.

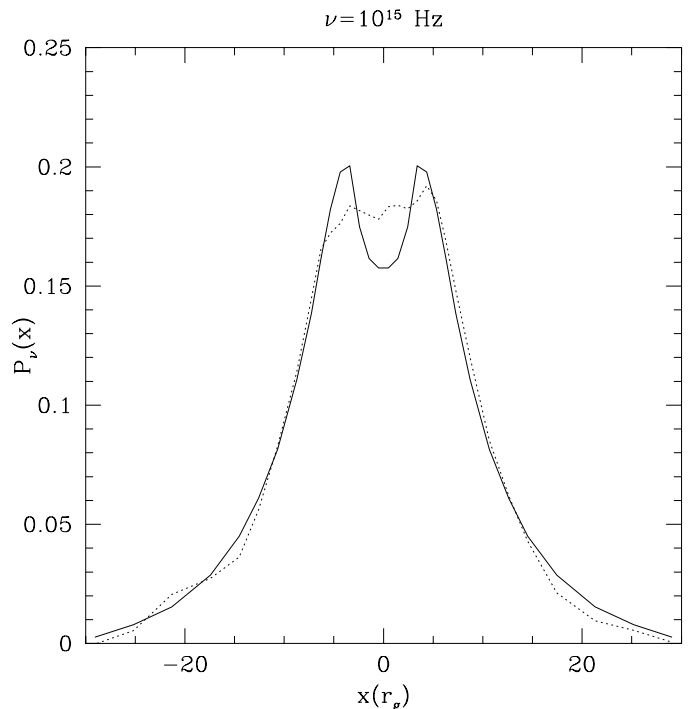


Fig. 1. Plot of recovered one-dimensional disk profile as a function of impact parameter for a face-on accretion disk using the Grieger et al. (1991) technique. Solid line is the model profile; dotted line is recovered profile. The parameter  $\alpha$  is distance across the source perpendicular to the caustic line in units of gravitational radii.

### 1.2. High magnification microlensing event

The spectrum of a quasar as a function of time is a convolution of the lensing magnification with the surface brightness of the quasar. Near a fold caustic, two bright images merge (Schneider et al. 1992). The resulting magnification has the specific form:

$$A(x, t) = A_0 + \frac{K}{\sqrt{|x - v_c(t - t_0)|}} \Theta[x - v_c(t - t_0)], \quad (2)$$

where  $A_0$  is the magnification due to the additional images,  $x$  is the position on the quasar plane perpendicular to the caustic,  $K$  is the strength of the caustic [units of (distance)<sup>1/2</sup>],  $v_c$  is the speed of the caustic (assumed to be positive),  $\Theta$  is the step function [ $\Theta(x) = 1$  for  $x > 0$ , 0 otherwise], and  $t_0$  is the time at which the caustic crosses the  $x = 0$  point measured relative to the center of the lightcurve (Schneider & Weiß 1986). This equation is valid whenever the source size is small compared to the Einstein ring radius of the microlensing star. If that ratio is small, there is only a small probability of any of a number of problems that might invalidate equation [2]. The list of potential problems includes: 1) the possibility that the source is projected behind a cusp (where the caustic curve discontinuously changes direction) or behind the crossing of multiple fold caustics; 2) significant curvature in the caustic; 3) variation of  $K$  along the caustic on the scale of the source. Grieger et al. (1988) demonstrate that a source of size smaller than  $\sim 10\%$  of the Einstein radius of the typical lensing mass is necessary for the second and third assumptions to be valid.

### 1.3. Microlensing Laboratory: The Einstein Cross

The Einstein Cross is a quasar ( $z=1.695$ ) lensed into four images by a nearby ( $z=0.0394$ ) barred spiral galaxy (Huchra et al. 1985). The luminosity distance to the quasar is  $D_L = 3 \times 10^{28} h_{75}^{-1}$  cm, where  $h_{75} = H_0/(75 \text{ km/s/Mpc})$ , assuming  $\Omega_m = 1, \Lambda = 0$ .

This quasar has been observed to undergo fluctuations due to microlensing roughly once per year (Irwin et al. 1989; R. Webster, private communication). It is particularly well suited for studying microlensing because the lensing galaxy is nearby. This happy coincidence makes the time delays between the four images all less than a day, so that it is easy to distinguish intrinsic variability from microlensing variability. It also makes the stellar velocities projected onto the source plane quite high, so that microlensing is frequent, and also makes individual events comparatively brief (only about a month, in contrast to the years to decade timescales characteristic of more distant lenses). In addition, the Einstein radius projected onto the quasar plane is quite large compared to the quasar size, validating the assumptions made in the previous subsection, and also making the microlensing variations strong.

The models of Witt et al. (1993) suggest that for image A,

$$\langle K \rangle \simeq 8 \left( \frac{r_E}{5.8 \times 10^{16} \text{cm}} \right)^{\frac{1}{2}} M_9^{-\frac{1}{2}}, \quad (3)$$

where  $r_E = 5.8 \times 10^{16} \text{cm} (m/0.2)^{1/2} h_{75}^{-1/2}$  is the Einstein radius projected to the quasar plane (Schneider et al. 1992),  $m$  is the typical mass (in Solar units) of a star causing microlensing, and  $M_9 = M_{BH}/10^9 M_\odot$ . In equation (3), and in the rest of the paper, we adopt  $r_g \equiv GM/c^2$  as the unit of distance. For concreteness, we will use  $K = 8$  in our simulations. The parameter  $A_0$  can be approximated by  $\langle A_0 \rangle = |(1 - \sigma)^2 - \gamma^2|^{-1}$  where  $\gamma$  is the shear (Witt et al. 1993). For image A, the estimated range of the microlensing parameters is  $\sigma = 0.3 - 0.4$  and  $\gamma = 0.4 - 0.5$ , giving  $A_0 = 3 - 9$ ; we use  $A_0 = 6$  in our simulations.

## 2. MICROLENSING OF AN ACCRETION DISK

### 2.1. Caustic crossing

As the caustic crosses the quasar, the observed lightcurve is a convolution of the magnification, equation [2] and  $P_\nu(x)$ :

$$F_\nu(t) = \int_{-\infty}^{\infty} A(x, t) P_\nu(x) dx. \quad (4)$$

Note that if the flux within a waveband can be measured outside of the caustic and subtracted off, then the dependence on  $A_0$  disappears, and the  $K$  parameter becomes degenerate with an arbitrary scaling of  $P_\nu(x)$ . As discussed by Grieger et al. (1991), equation [4] can be inverted using regularization to find  $P_\nu(x)$ . Similar techniques have been used for measuring the limb-darkening of stars during galactic microlensing events (Gaudi & Gould 1998, Albrow et al. 1998).

### 2.2. Black Hole geometry

Near a black hole, relativistic effects cause Doppler beaming of the emitted radiation, gravitational red shifts,

and bending of photon trajectories. To image the surface of an accretion disk, these relativistic effects must be accounted for using a relativistic transfer function (defined in Cunningham 1975). To compute the transfer function (see equation [5] below), we make several simplifying assumptions: (1) the accretion disk is thin, i.e.  $h \ll r$ ; (2) the gas follows prograde circular orbits outside the marginally stable radius  $r_{ms}$ , and undergoes freefall within  $r_{ms}$  with constant angular momentum and energy equal to those obtaining at  $r_{ms}$ ; (3) the disk is flat and lies in the equatorial plane of the black hole; (4) the gas emits isotropically in its rest frame, i.e., there is no limb darkening in the accretion disk atmosphere. The first two assumptions are appropriate if pressure gradients cause forces much smaller than the gravitational force in the  $z$  and  $r$  directions, respectively. This condition is not met in advection-dominated accretion flows or slim accretion disks (Beloborodov 1998). In the case of slim accretion disks, the orbital frequency is nearly Keplerian, and deviates by less than 20% when  $\dot{M}c^2/L_{Edd} \leq 1000$ ; however, the disk scale height can become a large fraction of the radius, which changes the emitted angle of radiation relative to the disk normal and can cause shadowing which we do not take into account. The third assumption is inappropriate if the disk is warped; however, Bardeen-Petterson precession (1975) can align the disk and black hole by the time the gas reaches the inner radii. The fourth assumption is a simplification for greater ease in the inversion computation since the disk can be viewed from only one angle and thus at most one emitted angle can be observed at each radius/azimuth of the disk. For each radius, there is a limited range of emitted angles which are observed, so our inversion will give some sort of average of the intensities within that range.

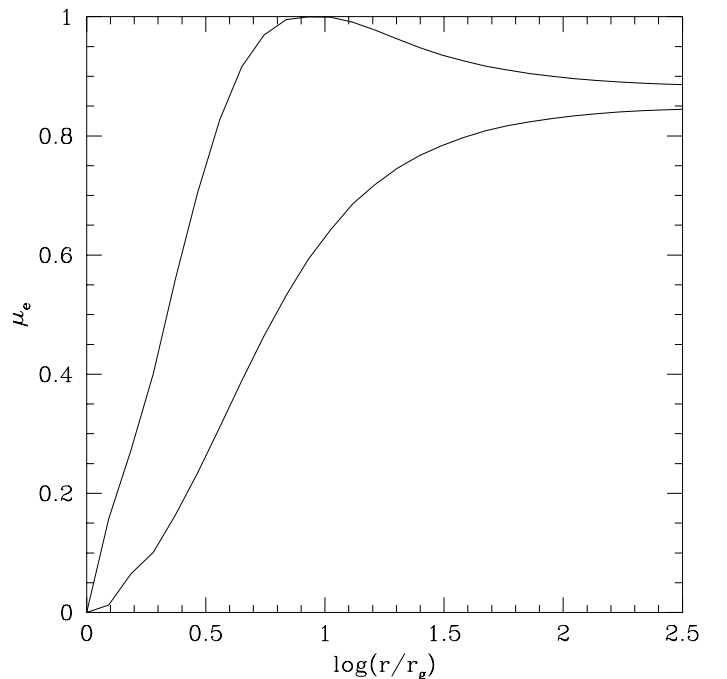


Fig. 2. The upper curve shows the maximum  $\mu_e = \cos \theta$ , where  $\theta$  is the angle between the disk normal and the direction of the photon in the fluid rest frame. The lower curve shows the minimum  $\mu_e$ . The disk parameters are

$i = 30^\circ$  and  $a_s = 0.998$ .

Figure 2 shows the range of emitted angles (in the fluid rest frame,  $\mu_e$  is the cosine of the normal to the disk) for a disk inclined at  $30^\circ$ . For a face-on disk, only one emitted angle is seen at each radius for all azimuths, so this assumption simply corresponds to mapping the specific intensity of the disk at  $\mu_e(r)$ . We could have assumed some limb-darkening law, but this is not warranted by the crudeness of the inversion technique.

Figure 3 shows the disk geometry. The inclination angle of the accretion disk,  $\mu = \cos i$ , is  $i = 0^\circ$  when the disk is face-on, and  $90^\circ$  when the disk is edge-on. The caustic crossing angle  $\phi_c$  is measured with respect to the  $(\alpha, \beta)$  coordinates, which are defined so that the  $\beta$  coordinate lies parallel to the projection of the disk axis onto the sky plane (in Figure 3, the disk spin axis is pointing out of the page), with the black hole at the origin. We will use units of  $r_g$  for the  $(\alpha, \beta)$  coordinates.

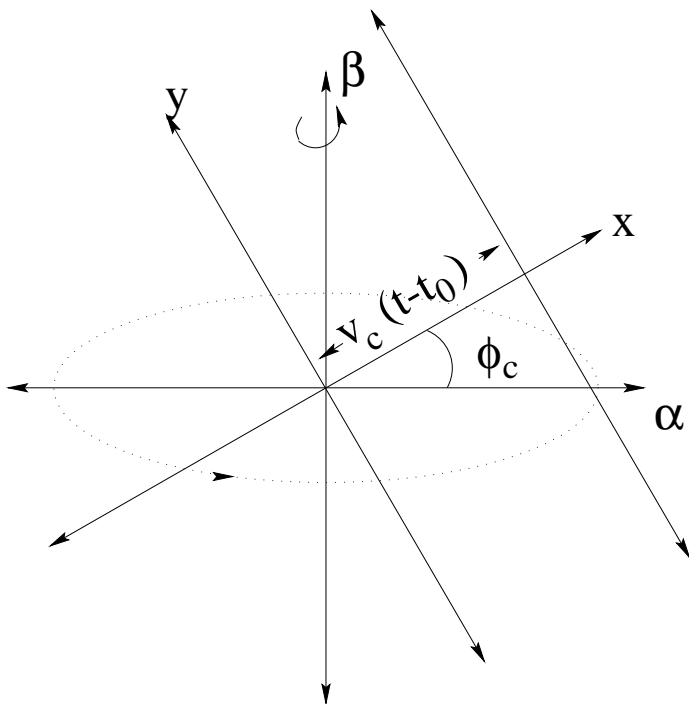


Fig. 3. Geometry of the accretion disk. The disk axis points up out of the page, while the  $\beta$  axis lies in the page. The line parallel to the  $y$  axis is the caustic.

The rotation of the accretion disk causes beaming of the radiation, leading to a hot spot on the approaching side, and a cold spot on the receding side. For an exactly face-on disk, the disk is symmetric, so no hot/cold spots exist, but a dip occurs inside the inner edge of the disk. In Figure 4 we show  $P_\nu(x)$  for a blackbody accretion disk at two frequencies. As the disk becomes more edge-on, the profile becomes more asymmetric as the Doppler aberration becomes stronger. If the temperature of the disk decreases outwards, then the size of the hot spot will increase for smaller frequencies, and become less asymmetric, as can be seen by comparing Figure 4(a) and 4(b). Figures 4(c) and 4(d) show  $P_\nu(x)$  for different caustic crossing angles,

showing the hotspot is oblong.

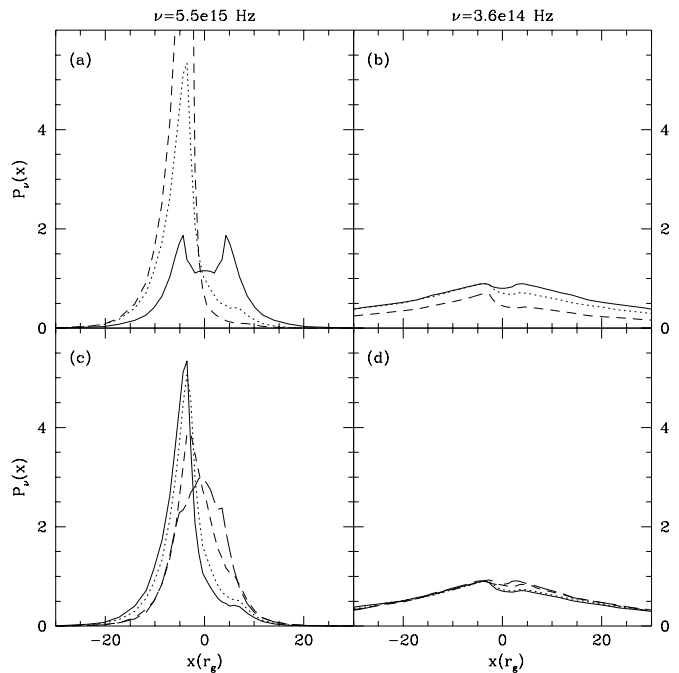


Fig. 1. Plots of the disk 1-D profile for a disk with  $M_9 = 1$ ,  $\dot{m} = 1$ , and  $a_s = 0.998$ . Figures (a) and (b) compare inclination angle:  $i = 0^\circ$  (solid),  $30^\circ$  (dotted) and  $60^\circ$  (dashed) for  $\phi_c = 0$ . Figures (c) and (d) compare  $\phi_c = 0$  (solid),  $30^\circ$  (dotted),  $60^\circ$  (short dashed),  $90^\circ$  (long dashed) for  $i = 30^\circ$ . The frequencies are in the quasar rest frame.

### 2.3. Prediction of the Lightcurve

With these assumptions and parameter choices, the observed flux may be predicted from the run of intensity with radius:

$$F(\nu_o, t) = \int d\alpha d\beta A [x(\alpha, \beta), t] g^3 I(\nu_o/g, r_e), \quad (5)$$

where  $g = \nu_o/\nu_e$  is the redshift between the observer and the emitter and  $I(\nu_e, r)$  is the specific intensity at the accretion disk (we have assumed it is independent of the emitted angle). The relation between the caustic coordinate and the black hole coordinates is  $x(\alpha, \beta) = \alpha \cos \phi_c + \beta \sin \phi_c$  (see Figure 3). The physical variables  $\nu_e$  and  $r_e$  may be related via a Jacobian to  $\alpha$  and  $\beta$  through their functional dependence on redshift  $g(\mu_o, a_s)$ , the inclination angle of the disk  $\mu_o$ , and the black hole spin  $a_s$ . The magnification  $A$  depends on  $\nu_c$ ,  $t_0$ ,  $\phi_c$ ,  $K$ , and  $A_0$ , for a total of seven model parameters.

We compute the transfer function by shooting rays from infinity at a grid in  $(\alpha, \beta)$  until they cross the equatorial plane. The computational method is based on Rauch & Blandford (1994), and is described in Agol (1997). We use a nested grid of rays that is more finely sampled towards the center to resolve the inner parts of the accretion disk in greater detail. For a given observed frequency  $\nu_o$ , we compute  $\nu_e$  as well as the emitted radius at each  $(\alpha, \beta)$ , and interpolate these on the (pre-specified) grid of radii and frequencies at the accretion disk.

To compute a normal transfer function, we would then simply sum over the grid. In this case, we multiply each ray by a further factor that describes the magnification due to the microlensing at any particular time, and then sum over the grid. This procedure may be summarized

$$F_i = T_{ij}I_j, \quad (6)$$

where  $i = 1, N_F$  ( $N_F = N_t \times N_\nu = \#$  observed frequencies  $\times$   $\#$  observed times) labels each measured observed frequency/time, and  $j = 1, N_I$  ( $N_I = \#$  emitted frequencies  $\times$   $\#$  emitted radii) labels each emitted frequency/radius pair. The matrix  $\mathbf{T}$  contains the integration and interpolation factors.

#### 2.4. Regularized Inversion

Attempting to directly invert equation [6] for  $\mathbf{I}$  given an observed set of  $\mathbf{F}$  is impossible since the matrix  $\mathbf{T}$  is generally singular, so that noise in the lightcurve is magnified strongly during inversion. This fact requires the introduction of some sort of *a priori* knowledge in order to make inversion feasible. Regularization is a particularly useful way to do this, as discussed in Press et al. (1992), because the “prejudice” injected into the solution is usually relatively benign and also relatively controllable. The essence of the linear regularization method is to minimize both the deviation of the model from the data, and also the deviation of the model from “smoothness,” as defined by some sort of differencing operator. In our case, at any given frequency, we expect the emitted intensity  $I_\nu$  to be smooth as a function of radius, but not the one-dimensional profile  $P_\nu$ .

In our specific implementation of the method, we also impose several other restrictions on the solution. We expect that the emitted intensity in the fluid frame diminishes as the black hole event horizon is approached; we therefore require  $I_\nu(r)$  to approach zero as  $r$  approaches  $r_g$ . In fact, because those regions are so strongly redshifted from almost any inclination angle, the intensity in the fluid frame is almost completely unconstrained by the data, so physical assumptions have a very strong impact on the solution in this region. Similarly, we also require  $I_\nu$  to approach zero at very large radii, for there is little energy available there to dissipate. Particularly at low frequency, it may sometimes be desirable to relax this constraint. In addition, we would like the inverted intensities to be positive definite; to achieve this, we maximize  $A_I = (\sum_i I_i w_i)/N_I$ , where  $w_i$  is a weighting factor. The most appropriate weighting is  $w_i = r_i^2$  since the radiating area associated with each logarithmic radius interval scales as  $r_i^2$ . Finally, for any choice of grid, there will always be some radius/emitted frequency pairs that are not constrained by the data because Doppler shifts push  $\nu_o$  outside the observed region (these are the intensities for which the corresponding column of  $\mathbf{T}$  is all zeros). In order to prevent those frequencies from contributing to the smoothing condition, we require that the associated intensities be zero.

Combining all these considerations leads to the following regularization operator:

$$\mathcal{B} = \frac{1}{A_I^2} \left\{ \sum_{i=N_\nu+1}^{N_I} (I_i w_i - I_{i-N_\nu} w_{i-N_\nu})^2 + N_I (I_1 w_1)^2 + \right.$$

$$\left. N_I (I_{N_I} w_{N_I})^2 + N_I^4 \sum_{\{j: \text{if } T_{ij}=0 \forall i\}} (I_j w_j)^2 \right\} \quad (7)$$

where  $N_\nu$  is the number of frequency grid points at the accretion disk. The first sum describes the smoothness as a function of radius at each frequency, the two isolated terms give the boundary conditions at the innermost and outermost radii, and the last sum is the factor encouraging minimization of those  $I_j$  unconstrained by data. Note that the specific intensity vector is ordered with all the frequencies at one radius grouped together, so that  $I_i$  and  $I_{i-N_\nu}$  give the intensity at the same frequency, but adjacent radii. The smoothing operator  $\mathcal{B}$  has the useful property of providing a model-independent measure of the “smoothness” of different solutions, due to the normalization by  $A_I$ . Other differencing schemes might also be used; in the examples we have explored, it makes little difference to the outcome.

Although the regularization condition is designed to be relatively innocuous, no such injection of prejudice can be altogether free from consequences (we will discuss the effect of our particular choice in §3.2). We stress that the details of the regularization condition are always subject to “tuning” in the light of either theoretical expectations, or, better, the implications of real data.

To solve for  $\mathbf{I}$ , we minimize the following function:

$$f(\mathbf{I}) = \frac{1}{N_F} \chi^2 + \lambda \mathcal{B} \quad (8)$$

with

$$\chi^2 = \sum_{i=1}^{N_F} \left( \frac{\sum_{j=1}^{N_I} T_{ij} I_j - F_i}{\sigma_i} \right)^2, \quad (9)$$

where  $\lambda$  is a constant, and  $\sigma_i$  is the error on  $F_i$ . We start with a direct solution of  $\partial f / \partial \mathbf{I} = 0$ , setting  $A_I = 1$ ,

$$\mathbf{I} = \left( \mathbf{M}^T \mathbf{M} + \frac{\lambda}{A_I} \mathbf{H} \right)^{-1} \mathbf{M}^T \mathbf{G} \equiv \mathbf{Q} \mathbf{M}^T \mathbf{G}, \quad (10)$$

where  $M_{ij} = T_{ij}/\sigma_j$ ,  $G_i = F_i/\sigma_i$ , and  $\mathbf{H}$  is defined such that  $\mathcal{B} = \mathbf{I} \cdot \mathbf{H} \cdot \mathbf{I}$ . We then update  $A_I$  from the solution, and iterate until  $A_I$  converges. In some instances,  $A_I$  can become negative after an iteration. If this happens, we reset  $A_I$  to be 0.1 times its value at the previous iteration, and recalculate the step.

We assume that the magnification outside the caustic,  $A_0$ , can be measured from the lightcurve, and subtracted off. Then, the parameter  $K$  (the caustic magnification factor) is completely degenerate with the disk surface brightness since a decrease in magnification corresponds to an increase in the surface brightness of the source. Consequently, we can determine the *shape* of the surface brightness profile, but not its absolute level.

Several other parameters also remain to be determined after the direct inversion for the surface brightness profile. We call them collectively  $\zeta = (t_0, v_c, \mu, \phi_c, a_s)$ . To find them, we fix  $\lambda$  and compute  $\chi^2$  over a coarse grid in this five-dimensional parameter space. Starting from the  $\zeta$  giving the smallest  $\chi^2$  in this grid, we refine our estimate of these parameters using the Levenberg-Marquardt method.

We compute the partial derivatives of  $\chi^2$  with respect to the axes in  $\zeta$  space by finite differences. If a parameter with boundaries goes out of bounds, we fix it at the value where it went out of bounds, and keep it fixed throughout the rest of the minimization. This generally occurred with  $a_s$  when it was near 0 or 1, and for  $\mu$  and  $\phi_c$  when the disk was face-on. Fixing this improved estimate for the best-fit  $\zeta$ , we increase  $\lambda$  and re-solve for the surface brightness profile until  $\chi^2 = N_F$ .

The number of degrees of freedom against which to compare  $\chi^2$  is not clearly defined for several reasons. One is that many of the model parameters are not entirely free; for several ( $\mu$ ,  $M_{BH}$ ,  $v_c$ ) there are prejudices or constraints from other experiments. Another reason is the variable weight given the smoothing constraint *vis-a-vis* the data, as we are minimizing  $\chi^2 + \lambda\mathcal{B}$  rather than  $\chi^2$ . In the limit of large  $\lambda$ , there is effectively only one free parameter for each frequency in the fit to the  $I_i$ ; in the limit of  $\lambda = 0$ , there are as many free parameters as there are grid points. Given these considerations,  $N_F$  is an upper bound to the true number of degrees of freedom; by raising  $\lambda$  until  $\chi^2 = N_F$ , we ensure that we do not overfit the data.

### 2.5. Errors

The word ‘‘error’’ has several different meanings in this context, and it is important to distinguish them. First of all, the errors in the inferred intensities have different properties from the errors in the model parameters. Second, both are potentially subject to systematic error as well as random error.

We will begin by estimating the random error in the intensities  $\mathbf{I}$ . Formally, we may say that

$$\delta I_i^2 = \sum_j \left( \frac{\partial I_i}{\partial F_j} \right)^2 \sigma_j^2, \quad (11)$$

where  $\frac{\partial I_i}{\partial F_j} = \sum_k Q_{ik} T_{kj} / \sigma_j^2$  (see equation [10]), and we assume the fluxes have uncorrelated errors. The  $\lambda = 0$  case is of special interest because it reveals which  $I_i$  (i.e., which frequency/radius pairs) are so constrained by the data that even without regularization they may be reliably determined. In this limit,  $\frac{\partial I_i}{\partial F_j} = T_{ij}^{-1}$ , so the uncertainty in  $I_i$  is given by  $\delta I_i^2 = W_{ii}^{-1}$  where  $W_{ij} = \sum_k T_{ki} T_{kj} / (\sigma_i \sigma_j)$ .  $\mathbf{W}^{-1}$  can be computed by singular value decomposition; in practice, we replace the singular values with a small number. We show an example of this procedure in Figure 9.

The ‘‘formal accuracy’’ of our inversion is illustrated by a plot of  $U_i \equiv I_i^r / \delta I_i$  (the superscript  $r$  stands for recovered intensity) as a function of frequency and radius, computed from equation [11] (Figure 9). The results for both  $\lambda = 0$  and the maximum  $\lambda$  consistent with the data are shown. In the case  $\lambda = 0$ , we use the original  $I_i$  instead of the recovered values to compute  $U_i$ . The formal accuracy depends on the true surface brightness: for a given radius,  $U_i$  tends to peak where the flux is largest. Also,  $U_i$  diminishes at large radii, since those radii aren’t monitored for long enough to truly determine  $I_i$ .

In real solutions  $\lambda \neq 0$ , and the smoothing operator correlates the intensities at neighboring radii sharing the same frequency. The uncertainties in this case are most

easily estimated by a Monte Carlo procedure in which the lightcurves are perturbed by random realizations of noise in the data. The distribution of  $I_i$  after re-solving each of these realizations gives the random error in  $I_i$ . In evaluating these estimates, it is important to understand that points weakly constrained by the data have little sensitivity to measurement errors because they are primarily determined by the smoothness constraint. As a result, their random errors are artificially small.

To check for systematic errors in the intensities, we will compute the difference between the original and recovered surface brightness,  $\Delta I_i = I_i^o - I_i^r$ , where superscript  $o$  stands for ‘‘original.’’ The systematic error is, of course, far more strongly model-dependent than the random error. It depends on the real intensity distribution, the character of the data (particularly the sampling), and the inversion scheme. These considerations will be discussed at greater length in §3.2.

We estimate the uncertainties in the model parameters  $\zeta$  two ways: through the same Monte Carlo procedure as for the  $I_i$ , and also through mapping out the  $\chi^2$  found by direct solution of the original data (at fixed  $\lambda$ ) for different choices of  $\zeta$ . Examples will be shown in §3.2, 3.3.

## 3. SIMULATIONS

### 3.1. Range of Parameters Examined

To determine how the inversion works in practice, we performed simulated inversions, varying the parameters describing the underlying model, the parameters describing the data set, and the parameters specifying the details of the solution technique. By varying the model parameters, we learn about whether the method is sensitive to the intrinsic nature of the quasar, or the microlensing event; by varying the observational parameters, we determine what the requirements will be for successful experiments; by varying the solution parameters, we learn how to tune the solution technique for optimum results.

#### 3.1.1. Model parameters $\zeta$

In all of our simulations we assume that the intrinsic radiated intensity in the fluid frame is a black body at the local effective temperature, isotropic in the outer half-space. Detailed non-LTE spectra computed for our fiducial parameters (see the next several paragraphs) are consistent with both the observed optical/ultraviolet spectrum and the microlensing size constraint for the Einstein Cross, given the freedom to choose an extinction correction and macrolens magnification (Hubeny & Agol, in preparation). However, we examined a number of possibilities for the other parameters defining the intrinsic character of the quasar and the microlensing events.

Although we do not know the mass of the black hole, we may set reasonable bounds on what it could be. If the intrinsic bolometric luminosity is  $3 \times 10^{46}$  erg/s (Rauch & Blandford 1991), the quasar would be at its Eddington limit if  $M_{BH} \sim 2 \times 10^8 M_\odot$ . On the other hand, the size of the optical emitting region is limited to no more than  $\sim 2 \times 10^{15}$  cm at  $\sim 10^{15}$  Hz (quasar rest frame) from microlensing (Wambsganss et al. 1990). If this equals the radius of maximum emission for an accretion disk ( $\sim 10 r_g$ ), then  $M_{BH} \sim 10^9 M_\odot$ . On this basis we suppose that the true mass is between  $2 \times 10^8 M_\odot$  and  $10^9 M_\odot$ . Our choice

for the fiducial model will be  $10^9 M_\odot$ .

The units we used in the simulations are  $r_g$  for length and  $\Delta t$ , the sampling rate, for time. The units of  $v_c$  are then  $r_g/\Delta t$ :

$$v_c = 0.29 \left( \frac{V_c}{5000 \text{ km/s}} \right) \left( \frac{M_{BH}}{10^9 M_\odot} \right)^{-1} \left( \frac{\Delta t}{1 \text{ day}} \right), \quad (12)$$

where  $V_c$  is the caustic velocity in km/s with distance measured at the quasar plane, while time is measured at the observer. The caustic velocity,  $V_c$ , is quite uncertain, but is likely to be in the range 3000–5000 km/s (Wyithe et al. 1999). For  $\Delta t = 3$  days, this corresponds to  $0.5 \leq v_c \leq 4$ , the range we span in our simulations. In the fiducial model, we choose  $v_c = 1$ .

We try values of  $\phi_c$  between 0 and  $2\pi$ , with  $\pi/2$  for our fiducial model.

We choose  $t_0 = 0$  for our fiducial model, and also try  $t_0 = 5$  to see whether this technique works when the central time of the monitoring does not coincide with passage of the caustic line across the center of the black hole.

There are no observational estimates of the inclination angle; however, unification arguments for radio-loud AGN suggest that quasars are less face-on than blazars, but closer to face-on than radio galaxies, so we choose a fiducial inclination of  $30^\circ$ . We also look at cases with  $\theta = 0$  and  $\theta = 60^\circ$ .

Because accretion can spin up black holes, and because Kerr holes permit more efficient accretion than Schwarzschild black holes, we choose  $a_s = 0.998$  for our fiducial model, but also study one example with  $a = 0$ .

The last parameter is the accretion rate. With the fiducial choices for the other parameters, the observed spectrum is best reproduced with  $\dot{m} \approx 1 = \dot{M}/(1M_\odot/\text{yr})$ .

### 3.1.2. Observational parameters

We vary the number of observations, time sampling interval, SNR, and number of observed wave bands, as well as the model parameters. It is especially important to determine how the quality of the result depends on the number of observations because these observations must be targets of opportunity, and thus will impact other observations at a given telescope. We explore what happens for experiments with between 5 and 41 observations (in all cases, we assume uniform spacing). The ratio between  $\Delta t$  and the duration of the microlensing event is implicitly given by  $v_c$ .

We try two choices for the SNR (as measured outside the microlensing event): 100 for each image in the best case, and 50 in the worst case (these were chosen based on current ground-based errors, Rachel Webster, priv. comm.).

Since disks are broad-band emitters, a broad range of observing frequencies is necessary. Observations in the four wave bands V, B, R, and I (or equivalent) should be routine; observations in U, J, H, K, or in the UV with HST will be much more difficult to obtain, but will yield much more information. To see just how important the additional bands are, we try using just ground-based data in 4 or 8 bands, or 8 ground + 3 HST bands in the best case. The short-wavelength bands are especially important for hot disks, since the deepest part of the potential well is seen at the shortest wavelengths.

### 3.1.3. Solution parameters

Several considerations determine the number of frequency and radius points at which we may solve for the surface brightness. The number of frequency points is not simply equal to the number of colors at which the quasar is monitored because of the extensive Doppler shifting. We found that in practice the best solution grids in both frequency and radius space were logarithmic. We solve for the intensity at frequencies equally spaced logarithmically between  $3 \times 10^{14}$  Hz and  $10^{16}$  Hz, and radii equally spaced logarithmically from  $r_g$  to  $r_{out}$ , with  $r_{out} = 500r_g$ . In the initial testing of the inversion using the fiducial model, we found the smallest number of radii and emitted frequencies for which we could obtain  $\chi^2 = N_F$  for some  $\lambda$  was 15 radii and 10 frequencies, which we subsequently used for all the simulations.

### 3.2. Best-case simulation

For our “best-case” simulation (designated A1 in Table 1), we fixed  $\zeta$  at the fiducial parameter choices. The observational parameters were: 41 observations,  $SNR = 100$ , and 11 spectral bands.

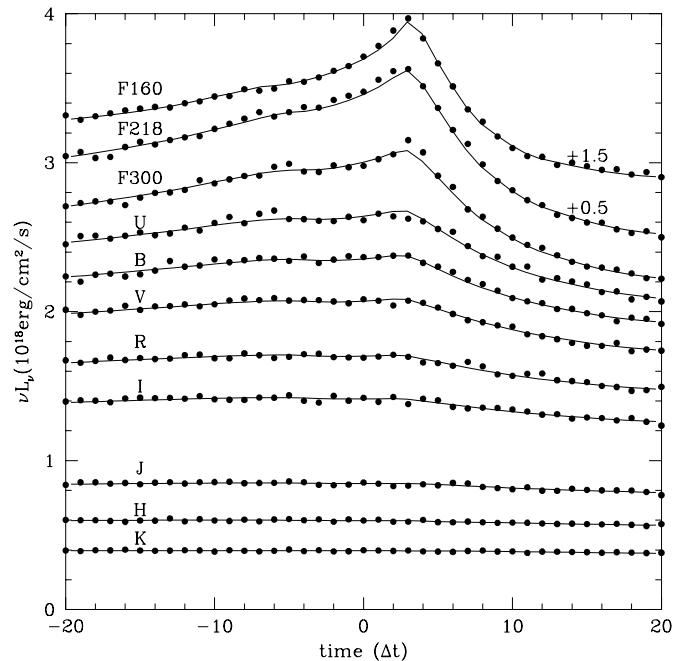


Fig. 5. Solid points are lightcurves with noise added. The top two curves have been shifted upwards by the amount indicated for clarity. The solid lines are the lightcurves from the reconstructed disk profile.

Figure 5 shows the lightcurves for this example, with the observed bands de-redshifted for  $z = 1.695$ . Note that the higher frequencies, which come from nearer to the black hole, are magnified more strongly than the lower frequencies. Figure 6 shows the original and reconstructed disk intensity,  $I(\nu_e, r_e)$ , as a function of frequency and radius for the best fit parameters for this best case (see Table 1). The overall shapes are reproduced quite well. Figure 7 shows the same results in a different format: we have multiplied surface brightness times  $r_e^2$ , and plotted the data

differently for clarity. Note that the low and high frequencies and small and large radii are poorly constrained since the simulated lightcurve only covers  $-20r_g < r < 20r_g$  and  $1600 \text{ \AA} < \lambda < 3 \mu\text{m}$ . Consequently, at these points the regularization tries to make the flux per log radius constant as a function of radius. Figure 8 shows the ratio of the reconstructed to the original one-dimensional profile,  $P_{\nu_o}(x)$  (computed from  $I_i^r$ ) for run A1.

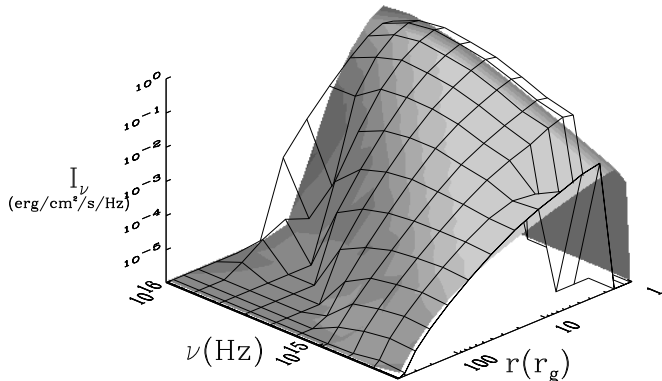


Fig. 6. Specific intensity  $I_\nu(r_e)$  versus emitted frequency and radius. The shaded surface is the original surface brightness, while the skeleton plot is the surface brightness recovered.

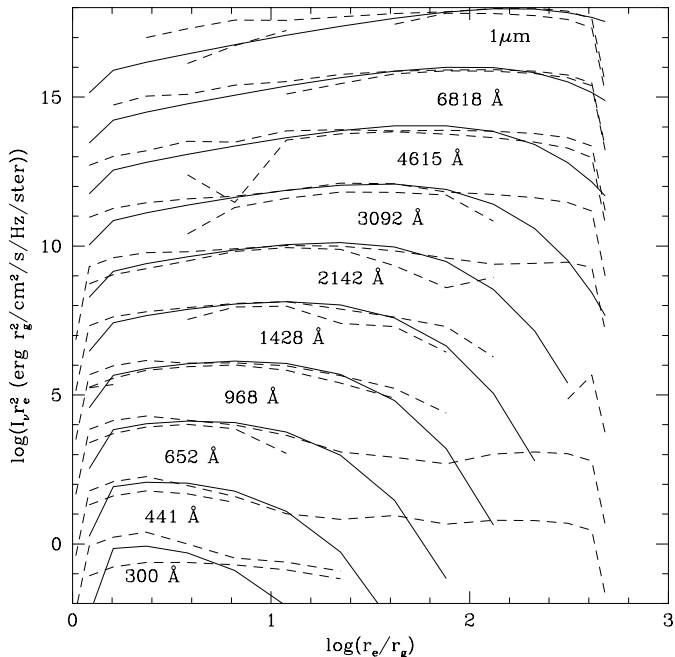


Fig. 7. Specific intensity  $I_\nu(r_e)$  times  $r_e^2$  versus  $r_e$  for each emitted frequency. The solid curves are the original  $I_\nu r_e^2$ , while the dashed curves are the minimum and maximum values of the recovered  $I_\nu r_e^2$  for 20 simulations. Each curve is shifted upwards by 2 with respect to the curve below - the zero point is for the lowest curve. We have not plotted negative intensities.

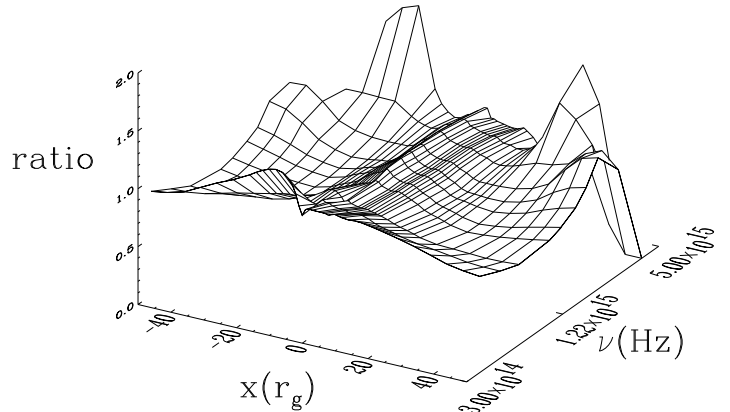


Fig. 8. Ratio of recovered to original one dimensional disk profile as a function of position and observed frequency.

To discuss the reliability of this solution, we begin by contrasting the region in the  $r_e - \nu_e$  plane where the random error is predicted to be relatively small with the region where the actual error is small. As can be seen in Figure 9, the region of large  $U_i$  for  $\lambda \neq 0$  largely, but not entirely, coincides with the region of large  $I_i^o/|\Delta I_i|$ . Moreover, both of these regions follow a track defined, not surprisingly, by the requirement that  $r_e^2 I_{\nu_e}(r_e)$  is relatively large. Elsewhere in the plane, the contribution to the flux is so small that the intensity is virtually unconstrained by the data.

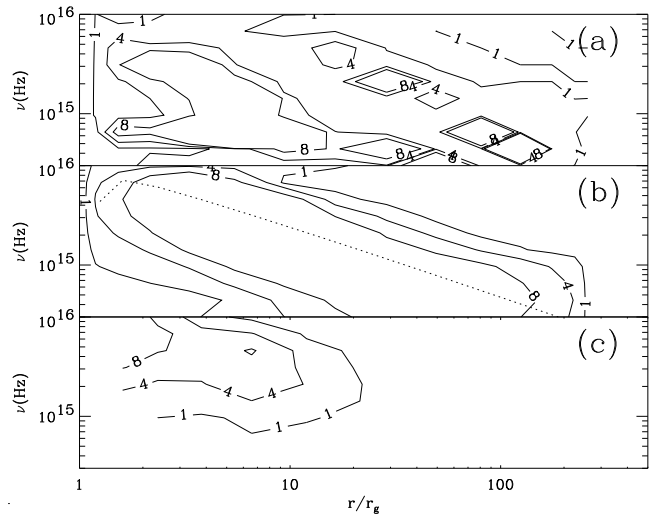


Fig. 9. Plot of  $I_i^o/\Delta I_i$  (a) and formal accuracy,  $U_i$ , of reconstructed disk profile for  $\lambda = 1.1$  (b) and  $\lambda = 0$  (c). The dotted line in panel (b) shows where the peak of  $B_\nu$  occurs at each radius.

Where  $U_i \simeq I_i^o/|\Delta I_i|$ , the error is predominantly random error, and  $\delta I_i$  is a good predictor of its magnitude (in fact, in this region  $\Delta I_i$  has a Gaussian distribution of the correct width). However, there is also a zone on the large radius side of the high-intensity track where the systematic error is as large or larger than the random error. The nature of this systematic error is revealed by studying Figure 7. The smoothing condition tends to raise the intensity in



regions where it should be small, and diminish it where it is large. Because  $U_i$  is rarely large enough to be interesting where  $I_i$  is small, it is the latter effect that dominates in the region of the  $r_e$ - $\nu_e$  plane highlighted in figure 9. At least within the context of this model, this systematic error is not the result of the specific choice of smoothing constraint: we have tried a second-order linearization scheme to see if we could get rid of the systematic deviation; however, we still found that the recovered intensity was flatter than the original. If we relax the condition that the intensity should be zero at the last radial bin, then the intensity approaches a constant for each frequency at large radius.

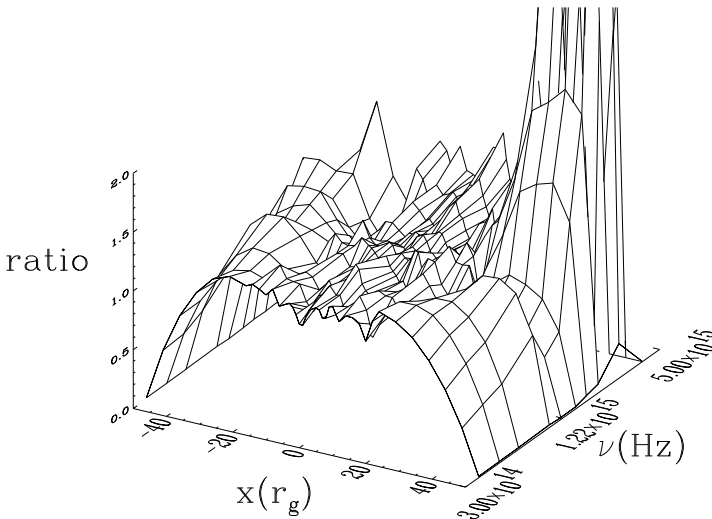


Fig. 10. Ratio of recovered to original one dimensional disk profile as a function of position and observed frequency, using the technique of Grieger et al. (1990).

We performed a regularized inversion using the Grieger et al. (1991) technique for comparison. Figure 10 shows their inversion on a data set equivalent to run A1. Since the regularization constraint attempts to smooth  $P_\nu$ , the Doppler peaks are smoothed over, and the noise from the lightcurve appears to still be present in the  $P_\nu$ .

After maximizing  $\lambda$  consistent with  $\chi^2 = N_F$ , we then fix  $\lambda$  and vary each component of  $\zeta$ , minimizing  $\chi^2$  with respect to the other parameters. This procedure shows how well each parameter can be constrained for a given simulation, or whether there are other local minima. In Figure 11 we show the  $\Delta\chi^2$  for each model parameter. For this particular model, the physically interesting parameters, inclination angle ( $\mu$ ) and caustic velocity ( $v_c$ ), have well-defined minima. The time of origin crossing ( $t_0$ ) and the caustic crossing angle ( $\phi_c$ ) are also well-behaved. The black hole spin has a rather flat  $\Delta\chi^2$  distribution. However, the minimum does lie at the correct value. Figure 11 also has a histogram of the parameters from each noise realization, showing that the minimum of the  $\chi^2$  distribution has few outliers.

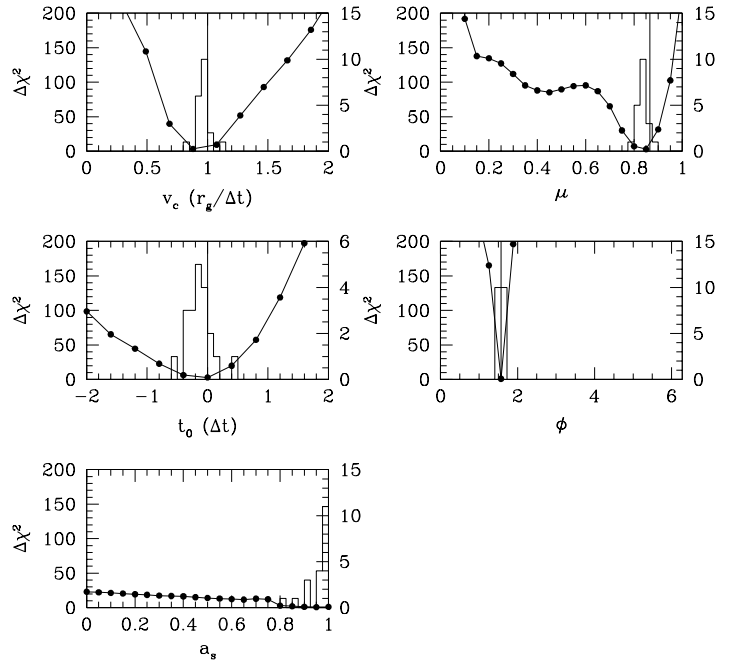


Fig. 11. Change in  $\chi^2$  versus each parameter for the A1 case. The vertical lines show the values of the original parameters. The histograms show the best-fit parameter results of 20 lightcurve realizations, with the right hand axis labelling the number in each bin.

### 3.3. Varying model parameters

Table 1 shows the results of varying the model parameters, keeping the observational parameters fixed at the “best-case” values.

Runs A1-A10 each have recovered surface brightness which look similar to A1, and the  $U_i$  are quite similar. Runs A11a and A12 reproduce the intensities well for the lowest frequencies and for radii outside  $r_{ms}$ ; however, the recovered intensities are non-zero inside  $r_{ms}$ , contrary to the input model.

Table 1 shows the average and standard deviation of the recovered parameters,  $\zeta$ , measured for 20 Monte Carlo realizations. In all the cases we examined, the distribution of recovered parameters is centered near the true model parameters, showing that there are no systematic offsets introduced by our inversion. This is encouraging since it means that this technique has the potential to measure important global properties of the accretion disk/black hole system.

Run A2 shows that we can determine the time that the caustic crosses the black hole rather accurately. We have also tried cases with  $t_0 = \pm 10$ , and we find that these are also measured quite well, and that the intensity is reproduced as well as in the A1 run.

Runs A3 and A4 show that we can distinguish between different caustic velocities, which means that we can constrain the black hole mass in terms of the lens velocity. Runs A5 and A6 show that we can measure the disk inclination angle for a wide range of intrinsic angles. Runs A7, A8, A9, and A10 show that we can measure the angle at which the caustic crosses the accretion disk rather accurately. In some cases there is a degeneracy between  $\phi_c$  and  $2\pi - \phi_c$  when the disk inclination is small, but this should not affect the recovered surface brightness since the disk

is approximately symmetric in this case.

Figure 12 shows the  $\chi^2$  topology for each parameter for Run A10, a somewhat special case in which  $\phi_c = \pi$ . The parameters  $t_0$  and  $\mu$  have local minima away from the correct minimum; however, these can be ruled out because some inferred intensities have large negative excursions in the false minimum.

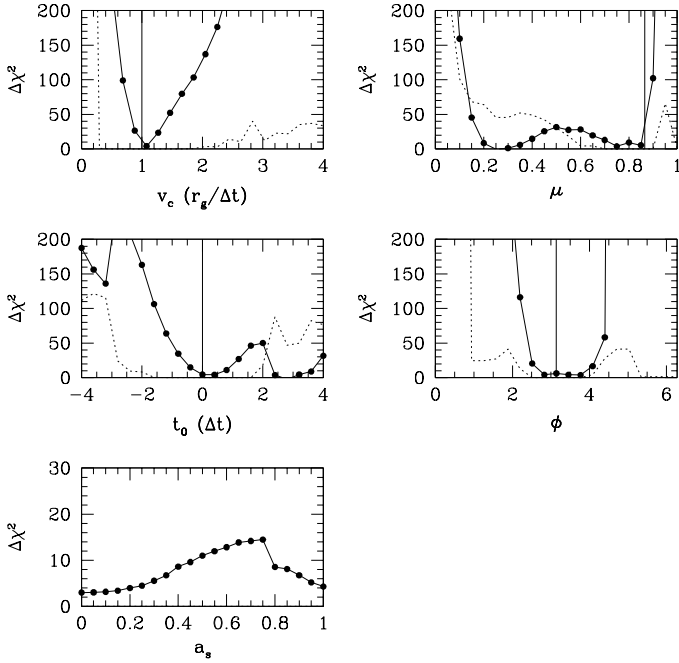


Fig. 12. Plot of  $\Delta\chi^2$  (minimized over all other parameters) vs. each parameter for run A10. The solid vertical lines show the original parameters. The dotted lines show the absolute value of the sum of the inverted intensities which are negative (the scale is from 0 to 1).

Constraining the spin can be difficult, particularly when  $\phi_c \simeq \pi$ . For example, in Run A10  $a_s$  is not constrained at all (see Figure 12).  $\chi^2$  has as deep a minimum at  $a_s = 0$  as it does at the correct value  $a_s = 0.998$ . Only if the coarse search in  $\zeta$  space is lucky enough to discover the true minimum will the Levenberg-Marquardt procedure home in on the correct value. It is not clear why some  $\phi_c$  are more favorable for determining  $a_s$ .

Whether  $a_s$  can be constrained at all depends on how strongly one believes in the model. If no emission is permitted inside the marginally stable orbit (Run A11b),  $a_s$  can be constrained because there is a sizable difference between the marginally stable orbit around a Schwarzschild black hole ( $6r_g$ ) and a maximal Kerr black hole ( $\simeq r_g$ ). However, if one is unwilling to make this assumption, the distinction between the spins largely disappears (Runs A11a and A12). The reason for this indistinguishability is shown in Figure 13, which shows a contour plot for the redshift as a function of position for black holes with spins  $a_s = 0.01$  and  $a_s = 0.99$ , including the regions inside  $r_{ms}$ . The two plots are almost identical around  $10r_g$ , where most of the observed radiation comes from in this model. Figure 14 shows the  $\chi^2$  (minimized over all other parameters) vs.  $a_s$  and recovered parameters for 25 simulations

assuming that emission only occurs outside of  $r_{ms}$ . The  $\chi^2$  has a clear minimum near the correct spin, and the simulations show that the spin can be rather accurately recovered. Since  $r_{ms}$  increases with decreasing spin, we can only hope to obtain a lower limit on  $a_s$  by assuming  $r > r_{ms}$ . Indeed, the  $\chi^2$  vs.  $a_s$  is flat in the case of zero spin (A11a).

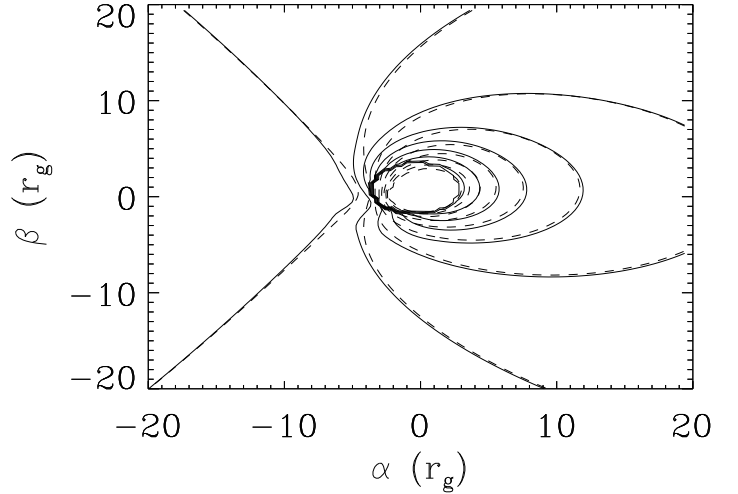


Fig. 13. Redshift as a function of position for black holes with spin  $a_s = 0.01$  (solid line) and  $a_s = 0.99$  (dashed line).

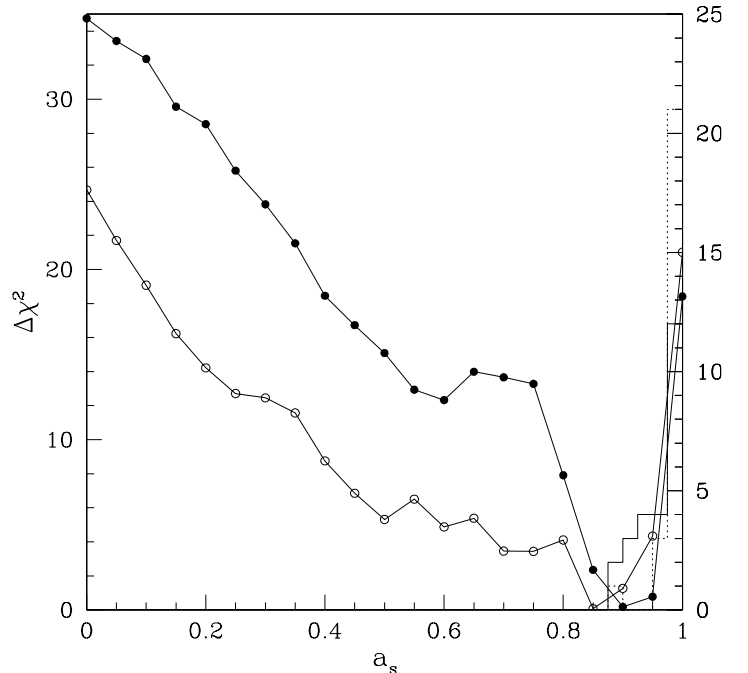


Fig. 14. Plot of the  $\chi^2$  vs.  $a_s$  (minimized over all other parameters) for cases A1 and A10, but with the additional assumption that emission only occurs outside  $r_{ms}$ . The solid dots show  $\chi^2$  for  $\phi_c = \pi/2$  (case A1) while the open circles for A10. The solid histogram shows the resulting  $a_s$  measured for 25 monte carlo simulations for A1; the dotted line for A10.

If the disk is much hotter than we have assumed, then

the parameters will not be as well constrained as those that we have used, as we would then sample only the outer regions of the disk. To illustrate this point, we have run a somewhat unrealistic model, A13, with the fiducial accretion rate, but a black hole mass of  $2 \times 10^8 M_\odot$  (near the Eddington limit). A standard blackbody accretion disk around a black hole with this mass cannot fit the observations as its spectrum is too steep and the magnification must be much larger than in standard models of the lens galaxy. The error on the measured spin is much larger than for Run A1 (see Table 2). The  $U_i$  for Run A13 are comparable to those in Run A1, so the intensities are recovered similarly well.

To see how well we can perform the inversion when the assumption of smooth radial variation is incorrect, we multiplied the accretion disk intensity by

$$1 + \sin \left[ 6\pi \frac{\log(r) - \log(r_{in})}{\log(r_{out}) - \log(r_{in})} \right], \quad (13)$$

which makes the disk three logarithmically spaced annuli (runs A14 and A15). Surprisingly, the recovered model parameters,  $\zeta$ , are accurate. Whether the radial variations can be discovered depends on the number of observations. In Run A14 (15 observations), the correct overall shape is found, but the radial modulation not reproduced; in Run A15 (41 observations), the radial dependence of the recovered intensities is more nearly correct. This indicates that the inversion is only accurate if our smoothness model assumption is met on the smallest scale probed by the sampling. Figure 15 shows the results of run A14.

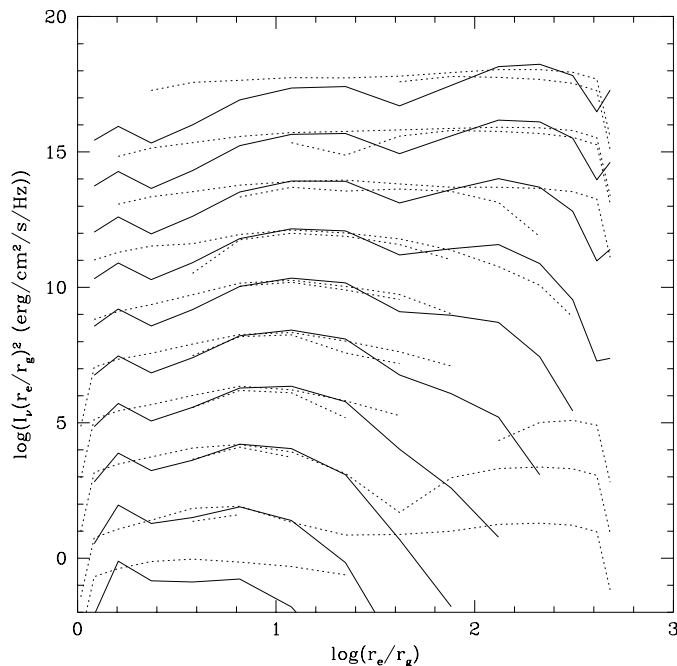


Fig. 15. Plot of original (solid lines) and recovered (dotted lines) for blackbody disk with fluctuations added (model A14). Each curve shows a different frequency (from  $3 \times 10^{14}$  to  $10^{16}$  Hz), shifted by 2 units for clear separation. The dotted lines show the maximum and minimum recovered intensity from 20 Monte Carlo realizations, with only positive intensities plotted.

We have not tried breaking the assumption of azimuthal symmetry, as the transfer function is computed assuming it.

### 3.4. Varying observation parameters

The question of how many observations are necessary is addressed with Runs M2a-d (Table 2). First, we compare fewer observations (21) at the same sampling rate (M2a) and for the same duration (M2b). In each case, the rms scatter of the model parameters is remarkably small compared to Run A1. Thus, *if the underlying model is correct*, it appears that we can determine the model parameters with a high degree of accuracy with relatively few observations.

A smaller number of observations, however, impairs our ability to reconstruct the true surface brightness of the accretion disk, as the inversion relies more upon the smoothing constraint than on the actual data. This can be seen in Figure 16, which shows the derived formal accuracies for various numbers of observations.

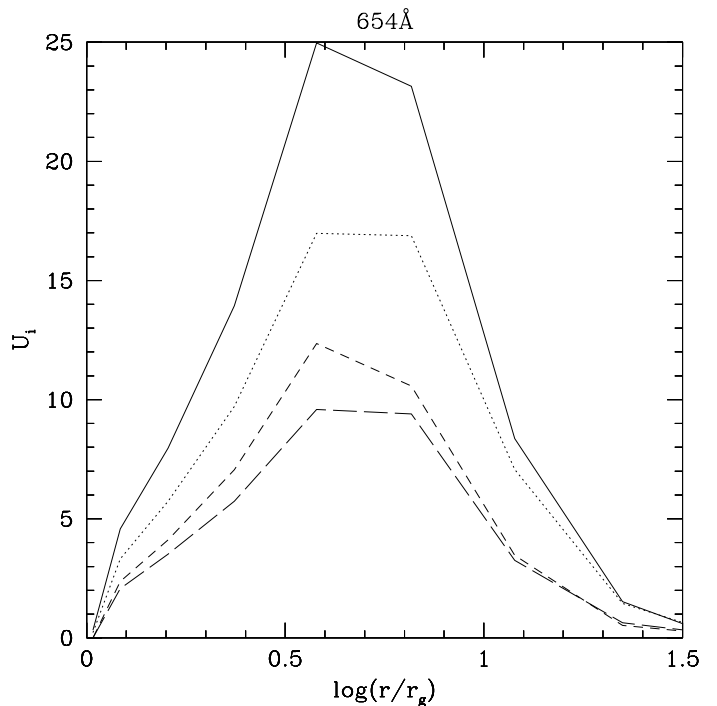


Fig. 16. This shows a plot of the  $U_i$  as a function of radius for various numbers of observations at a single frequency: solid line is  $N_t = 41$  (A1), dotted line is  $N_t = 21$  (M2b), short-dashed line is  $N_t = 11$  (M2d), and long-dashed line is  $N_t = 5$  (M2e).

The total amount of information about the intensities that may be gleaned also depends on the number of observations. It is obvious that the number of frequencies at which the intensity may be inferred scales in proportion to the number of bands whose lightcurves are measured. In addition, comparing A1 with M2b-d shows that the number of radial points with reliable solutions increases slowly with increasing number of observation times  $N_t$ . This is because each observation constrains most strongly the minimum radius where the caustic crosses. Since the

observations are spaced linearly, while the radii are spaced logarithmically, the number of radial points constrained by the data is  $\propto \log(r_{max}/r_{min}) \propto \log(T/\Delta t) \propto \log(N_t)$ , where  $T$  is the total duration and  $r_{max}$  and  $r_{min}$  are radii corresponding to the radial limits of the region with a reliable solution. In addition,  $U_i \propto N_t^{1/2}$  (see Figure 16), in the usual fashion of signal-to-noise ratios.

In addition to the number of observations, the SNR of each observation affects the quality of the inversion. Runs M3a-b with SNR=50 demonstrate this dependence. For Run M3a, the recovered parameters have similar errors to those in Run A1, except for the errors on the spin. For Run M3b, the errors on recovered parameters are roughly double those in Run M2d. For fixed model parameters and fixed number of observations, on average the errors on  $\mathbf{I}$  are directly proportional to the errors on  $\mathbf{F}$ ; in other words,  $\langle U_i \rangle \propto SNR$ , where the average is over 20 simulations. For individual simulations, the  $U_i$  depend on  $\lambda$ , which causes scatter in  $U_i$ .

Next, we look at the dependence of the solution on which frequencies are observed. Run M4a shows that the best fit model parameters,  $\zeta$  are not strongly dependent on the infrared frequencies. However, excluding infrared bands reduces  $U_i$  at the lowest frequencies. Run M4b shows that the best fit  $\zeta$  are strongly dependent on observing the ultraviolet frequencies. This run has the largest errors on model parameters and poorest agreement with the true parameters. In addition, the  $U_i$  at the highest frequencies are strongly reduced for this run. Comparing Runs A1, M4a,b, we find that the number of frequencies (at the accretion disk) constrained by the data  $\propto N_\nu$ , which shows why broad frequency coverage is crucial for mapping out the disk spectrum.

Runs A1, A3, and A4 show that both the number of radial points with reliable recovered intensities and  $U_i$  are insensitive to the total duration of the monitoring within the range of uncertainties in  $v_c$ . Runs A2 shows that the time at which we begin the observations does not strongly affect the derived parameters or surface intensity, as long as we catch the region near the peak.

## 4. DISCUSSION

### 4.1. Observational requirements

Experimental design depends on which questions are the goal, and to what accuracy one aims to answer them. Consequently, this discussion, much like our earlier discussion of the experimental errors, divides according to whether the primary aim is to map the surface brightness of the disk, or to infer the model parameters.

If the goal is to obtain a map of the the disk intensity as a function of radius and frequency over as large region in the  $r_e$ - $\nu_e$  plane as is possible, it pays most to invest in multiple monitoring bands because the number of radius-frequency pairs for which it is possible to find a solution is  $\propto N_\nu$ , but rises only logarithmically with  $N_t$ . We expect the intensity to vary as a power law in radius, so a better observation strategy might be to space observations logarithmically in time; however, this will be difficult to achieve in practice, which is why we have assumed equal time spacing. The accuracy of the solution is directly proportional to the SNR in the data. To map the regions nearest to the black hole, the highest UV frequencies are crucial (although this de-

pends on the assumption that the spectral peak moves to higher frequencies at smaller radii); however, lower frequencies are required if one is interested in obtaining a broad-band spectrum. Note also that a higher sampling frequency increases the chance that one will obtain monitoring data during the time when the caustic line is near the black hole. To obtain high formal accuracy for a broad range in radius requires a lightcurve that is finely sampled for a long time period. To determine the intensities, the model parameters must also be well-defined. When the observations are too few or the SNR too small, the uncertainties in  $\zeta$  contribute to the uncertainty in  $I_i$ .

If the goal is to simply constrain the model parameters, and one believes that the model is correct, then only a small number of observations may be required (5 observations were sufficient in our simulations to constrain all model parameters to better than 20% at  $1\sigma$ ; 11 observations for  $\leq 10\%$   $1\sigma$  accuracy). Since the black hole mass and caustic velocity are quite uncertain, it may be necessary to have more observations to be sure to obtain the few near the peak of the caustic crossing that are essential for success. The highest frequencies are most important for constraining model parameters.

In our simulations we assumed that only statistical errors affected the fluxes, and that these errors can be estimated from the observational data. There might also be systematic errors in the fluxes due, for example, to emission line contributions, inaccurate calibration between bands, or cosmic rays. The quality of the result could also be affected by these problems.

### 4.2. Under what circumstances might the model fail?

The inversion scheme we propose assumes a model that is plausible—a geometrically thin relativistic accretion disk in which azimuthal variations are quickly smoothed out, microlensed by a caustic system whose basic length scale is much larger than the size of the bright region of the disk. However, we are by no means guaranteed that even this general framework is correct. In this section we discuss what would happen if our method is attempted, but one of these assumptions is invalid.

The most basic of our assumptions is that the surface brightness varies smoothly as a function of radius. Given sufficiently dense sampling with good SNR, even quite sharp gradients could be recognized by our procedure. On the other hand, if the sampling is inadequate, the existence of such features would appear only as a troubling inability to find a solution with adequate  $\chi^2$ , unless  $\lambda$  is taken to be very small.

Another potential source of trouble is departures from azimuthal symmetry. In the absence of microlensing, “spots” can modulate the lightcurve on the orbital period if they are in the relativistic portion of the disk and the inclination is relatively large (Abramowicz et al. 1991). In this case, that would mean periods of  $\simeq 31M_9(r/10r_g)^{3/2}(1+z)/2.7$  days (in the observed frame). Because the largest observed variations in the Einstein Cross are  $\sim 10\%$  on year-long timescales, this effect cannot be too strong in this system. However, there might be a range of spot brightness in which they are too weak to show up in the ordinary lightcurve, yet strong enough to cause some periodic modulation of the lightcurve during a microlensing event (Gould & Miralda-Escudé 1997). Because

the likely duration of a microlensing event (a few weeks) is several to ten times the orbital period for the brightest part of the disk, it is possible that this effect might be seen directly in the lightcurve. If not, they might still make it difficult to find a solution with acceptable  $\chi^2$ . Particularly if the break in azimuthal symmetry is approximately  $\propto e^{i\phi}$  and the disk is nearly face-on, a strong spot might be confused with Doppler boosting, leading to a mistaken inference for the disk inclination.

Several physical effects might make disks geometrically thick—radiation pressure support if the luminosity approaches Eddington (Abramowicz et al. 1988), gas pressure support if the ions retain most of their heat (Rees et al. 1982, Narayan & Yi 1995), or an optically thick outflow. If any of these mechanisms acts, the orbital velocity at the photosphere would no longer be that corresponding to circular free-fall in the equatorial plane of the black hole, so that the general relativistic transfer function we apply would no longer be valid. We would expect, then, difficulties in finding a solution with acceptable  $\chi^2$ , but the portion of our solution describing the outer regions of the disk should be only weakly affected.

The surface brightness model we have used for the inversion simulations is roughly consistent with both the observed spectrum (given the uncertainty in reddening) and the current microlensing size constraint, but it is not unique. If the actual spectrum has strong emission in the far ultraviolet (which could be true if the reddening is greater than our estimate), the observable portion of the spectrum will be dominated by emission far from the horizon, weakening all the relativistic effects. If so, the disk inclination and black hole spin will be poorly constrained.

Uncertain reddening can have other effects, also. Because we can expect it to be uniform across the face of the disk, it should not affect the inferred radial profile of the disk, but it could well introduce additional uncertainty into our estimate of the intrinsic disk spectrum at any given radius.

Our assumption that the bright part of the disk is small relative to the caustic length scale is unlikely to be broken, except in the outer regions of the accretion disk. In this case, for which the microlensing optical depth is  $\sim 1$  (Witt & Mao 1994), the caustic scale is essentially the size of the Einstein ring due to a single star. Consequently, the ratio between the disk size and the caustic scale is only  $\simeq 0.01 M_9 (r/10 r_g) m^{-1/2} (h/0.75)^{1/2}$ , where  $m$  is the mean mass of microlensing stars in Solar units, so according to the Grieger et al. (1988) criterion, the caustic assumption is likely to be valid out to  $100 r_g$ . In our fiducial model, for example, the flux at  $100 r_g$  peaks at an observed wavelength  $1[(1+z)/2.7] \mu\text{m}$ , where we have scaled to the redshift of the Einstein Cross.

However, there might be difficulties in practice from a related problem: measuring  $A_0 F_\nu$ . Again, if the disk size is much smaller than the Einstein radius of a single star, then  $A_0$  is approximately constant during a high amplification event; thus, the same criterion for success applies as in the previous paragraph. Of course, observations when the quasar is outside the caustic are still required to measure  $A_0$ . Given the expectation that the quasar is smaller at higher frequencies, observing at the highest frequencies will provide the best constraint on  $A_0$ . To determine how these difficulties and those listed in §1.2 will affect the

inversion, we are currently running simulations of full microlensed lightcurves appropriate for the Einstein Cross, to which we will apply our inversion algorithm (Wyithe & Agol, in preparation).

In any of these instances of model inappropriateness, the impact on specific inferred parameters depends somewhat on details of the inversion procedure. For example, if the procedure we have outlined is followed (i.e., minimizing  $\chi^2$  by varying  $\zeta$  at fixed  $\lambda$ , then raising  $\lambda$  until  $\chi^2$  meets our definition of acceptability), difficulty in achieving satisfactory  $\chi^2$  reduces the ultimate  $\lambda$ . This means that, in effect, more degrees of freedom are “spent” on fitting the  $I(r, \nu)$ , leaving fewer for defining  $\zeta$ . If the problem is lack of smoothness in the radial profile, this transfer of effort is reasonable; if the problem is different, however, and if one cares about the accuracy of the  $\zeta$  parameters, one might choose to modify the procedure in a way that keeps  $\lambda$  fixed at a relatively large value.

One disadvantage of using linear regularization is that the intensities are not required to be positive definite, though it is impossible to emit a negative number of photons. We have tried to incorporate this by trying three other methods: maximum entropy; replacing  $I_i$  by  $\log(I_i)$  in  $\mathcal{B}$ ; and the method of projections onto convex sets. Each technique finds solutions that are local minima with large  $\chi^2$ . Another useful technique might be to make the further assumption that the spectrum at each radius can be described as a blackbody, and then solve for the temperature as a function of radius. These methods are all non-linear, and thus intrinsically slow. They therefore impede the exploration of parameter space, but might be interesting for future work.

#### 4.3. Multiple microlensing events

Of the five parameters in  $\zeta$ , three ( $t_o$ ,  $v_c$ , and  $\phi_c$ ) will change from one event to the next, but the other two ( $a_s$  and  $i$ ) should remain fixed. Since we expect roughly one event per year, it should be possible to combine observations of several events in order to more tightly constrain  $a_s$  and  $i$ .

#### 4.4. Connection to X-ray microlensing events

The optical and ultraviolet continua of quasars are not the only portions of the spectrum radiated by the inner part of the accretion disk. The X-ray continuum must also come from somewhere near that region. It, too, should therefore be microlensed in much the same way as the optical and ultraviolet continuum we have discussed in this paper.

Whether the same technique can be successfully applied to the X-ray continuum depends on the same considerations as discussed in §4.2, but several of them are more likely to present problems in the context of X-rays than for the optical/ultraviolet continuum. There have been numerous suggestions, for example, that the X-rays are produced in a relatively small number of compact active regions (e.g., Haardt et al. 1994) that might have substantial velocities relative to the disk (Beloborodov 1999). If so, the assumptions of azimuthal symmetry, radial smoothness, and also simple circular orbital motion might all be suspect.

Nonetheless, it would certainly be worthwhile to monitor the X-ray flux during a microlensing event, in the

hope that its emissivity distribution is sufficiently consistent with our assumptions that it, too, could be mapped. Combining this data set with the optical/ultraviolet data would also provide an independent constraint on the  $\zeta$  parameters, which should all be the same for the same event.

#### 4.5. Summary

We have demonstrated that monitoring microlensing events in the Einstein Cross quasar has great potential for both revealing the structure of its continuum emission with unprecedented resolution, and potentially constraining such basic parameters of the quasar as the spin of its black hole (if we assume emission occurs only outside of the marginally stable circular orbit), the mass of the black hole (modulo the caustic velocity), and the inclination angle of its disk relative to our line of sight. If this potential is

realized, and the analytic method we have proposed is implemented successfully, we may be able to begin answering such fundamental questions as: What is the intrinsic local spectrum of the disk? How close is it to thermal? And, most fundamentally, does the dissipation distribution in accretion disks vary with radius in the fashion predicted (see equation 1) long-ago?

We would like to thank Andy Gould and Chris Kochanek for useful discussions. We thank Casey Pavovich, Keiichi Wada, Andrew Zirm, and Viktor Ziskin for time on their workstations. Thanks to David Heyrovsky and the referee for comments which improved the manuscript.

This work was partially supported by NASA Grant NAG 5-3929 and NSF Grant AST-9616922.

#### REFERENCES

- Abramowicz, M., Bao, G., Lanza, A. & Zhang, X. 1991, A & A 245, 454  
 Abramowicz, M., Czerny, B., Lasota, J.-P. & Szuszkiewicz, E. 1988, ApJ 332, 646  
 Agol, E., 1997, PhD Thesis, University of California, Santa Barbara  
 Albrow, M. et al., the PLANET Collaboration, 1998, ApJ submitted, astro-ph/981114 79  
 Bardeen, J. M. & Petterson, J. A., 1975, ApJ, 195, L65  
 Beloborodov, A. M., 1998, MNRAS, 297, 739  
 Beloborodov, A. 1999, astro-ph/9809383  
 Corrigan, R.T. et al., 1991, AJ, 102, 304  
 Czerny, B., Jaroszyński, M., & Czerny, M., 1994, MNRAS, 268, 135  
 Cunningham, C. T., 1975, ApJ, 202, 788  
 Gaudi, B. S. & Gould, A., 1998, ApJ, submitted, astro-ph/9802205  
 Gould, A. & Miralda-Escude, J., 1997, ApJ, 483, L13  
 Gould, A. & Gaudi, B. S., 1997, ApJ, 486, 692  
 Grieger, B., Kayser, R., & Schramm, T., 1991, A & A, 252, 508  
 Grieger, B., Kayser, R., & Refsdal, S., 1988, A & A, 194, 54  
 Haardt, F., Maraschi, L. & Ghisellini, G. 1994, ApJ 432, L95  
 Huchra, J., et al., 1985, AJ, 90, 691a  
 Irwin, M. J., et al., 1989, AJ, 98, 1989  
 Jaroszyński, M. & Marck, J.-A., 1994, A & A, 291, 731  
 Krolik, J. H., 1998, Active Galactic Nuclei, (Princeton: Princeton University Press)  
 Jaroszyński, M., Wambsganss, J., Paczyński, B., 1992, ApJ, 396, L65  
 Narayan, R. & Yi, I., 1994, ApJ, 428, L13  
 Page, D. N. & Thorne, K. S., 1974, ApJ, 191, 499  
 Press, W., Teukolsky S., Vetterling W., & Flannery, B., 1992, *Numerical Recipes in FORTRAN*, 2nd edition, (Cambridge: Cambridge University Press)  
 Pringle, J. E., 1981, ARAA, 19, 137  
 Rauch, K. P., & Blandford, R. D., 1991, ApJ, 395, L65  
 Rauch, K. P., & Blandford, R. D., 1994, ApJ, 421, 46  
 Rees, M. J., Phinney, E. S., Begelman, M. C., & Blandford, R. D., 1982, Nature, 295, 17  
 Schneider, P., Ehlers, J., & Falco, E., 1992, *Gravitational Lenses* (New York: Springer-Verlag)  
 Schneider, P. & Weiß, A., 1986, A & A, 164, 237  
 Wambsganss, J., Paczyński, B., & Schneider, P., 1990, ApJ, 358, L33  
 Wisotzki, L., Köhler, T., Kayser, R., and Reimers, D., 1993, A & A, 278, L15  
 Witt, H. J., Kayser, R., & Refsdal, S., 1993, A & A, 268, 501  
 Witt, H. J. & Mao, S., 1994, ApJ, 429, 66  
 Witt, H. J., Mao, S., & Schechter, P. L., 1995, ApJ, 443, 18  
 Wyithe, J. S. B., Webster, R. L., & Turner, E. L., 1999, astro-ph/9901341

TABLE 1  
 MODEL PARAMETERS FOR MONTE CARLO RUNS (FOR  $N_t = 41$ , SNR = 100, AND  $N_\nu=11$ )

Model	$t_0(\Delta t)$	$v_c(r_g/\Delta t)$	$\mu$	$\phi_c$	$a_s$	$\lambda$
A1	0 -.1±.2	1 .96±.06	0.866 .84±.02	$\pi/2$ 1.56±.03	0.998 .96±.05	.01-1.9
A2	5 -4.8±.2	1 .96±.06	0.866 .84±.02	$\pi/2$ 1.58±.02	0.998 .97±.03	.002-1.7
A3	0 -.10±.13	2 1.95±.095	0.866 .83±.03	$\pi/2$ 1.58±.03	0.998 .93±.08	.01-1.6
A4	0 -.18±.2	.5 .50±.02	0.866 .85±.02	$\pi/2$ 1.57±.02	0.998 .97±.03	.001-2.3
A5	0 -.06±.07	1 1.02±.04	1.0 .999±.001	n/a 1.53±.08	0.998 .99±.02	.0001-1.8
A6	0 -.03±.08	1 .95±.05	0.5 .50±.02	$\pi/2$ 1.57±.01	0.998 .92±.06	.005-1.8
A7	0 -.02±.13	1 .99±.04	0.866 .84±.01	$\pi/4$ .83±.05	0.998 .95±.11	.01-1.7
A8	0 -.03±.1	1 1.01±.03	0.866 .86±.01	$3\pi/4$ 2.33±.04	0.998 .99±.02	.003-1.9
A9	0 .1±.1	1 .98±.06	0.866 .84±.02	$3\pi/2$ 4.72±.02	0.998 .95±.05	.006-1.9
A10	0 .03±.07	1 1.03±.03	0.866 .86±.01	$\pi$ 3.16±.08	0.998 .99±.03	.005-1.8
A11a	0 -.46±.26	1 .95±.07	0.866 .78±.06	$\pi/2$ 1.57±.02	0. .17±.32	.005-.8
A11b <sup>a</sup>	-.22±.24	.87±.07	.87±.02	1.57±.02	.09±.12	.001-4.4
A12	0 -.29±.20	1 .91±.09	0.866 .83±.07	$\pi/2$ 1.57±.02	0.5 .55±.25	.03-.7

<sup>a</sup>We have constrained  $r > r_{ms}$ .

TABLE 2  
 MONTE CARLO PARAMETERS (FOR  $t_0 = 0$ ,  $\mu = .866$ ,  $\phi_c = \pi/2$ ,  $a_s = .998$  MODEL)

#	$N_t$	SNR	$N_\nu$	$v_c$	$v_c(\text{meas})$	$t_0(\Delta t)$	$\mu$	$\phi_c$	$a_s$	$\lambda$
A13 <sup>a</sup>	41	100	11	1	.93±.07	-.2±.4	.85±.04	1.58±.06	.89±.19	.01-2
A14 <sup>b</sup>	15	100	11	2.9	2.6±.3	-.04±.06	.90±.04	1.57±.03	.87±.19	.07-.9
A15 <sup>b</sup>	41	100	11	1	.98±.06	.05±.20	.88±.05	1.57±.02	.79±.20	.002-.18
M2a	21	100	11	1	.99±.04	-.13±.15	.84±.01	1.58±.02	.98±.05	.5-5.2
M2b	21	100	11	2	1.9±.13	-.12±.07	.82±.02	1.59±.03	.93±.07	.2-4.8
M2c	15	100	11	2.9	2.7±.3	-.09±.1	.83±.03	1.59±.03	.95±.06	.6-6.6
M2d	11	100	11	4	3.9±.3	-.03±.07	.83±.03	1.56±.03	.9±.1	1.7-11
M2e	5	100	11	10	8±2	0.±.15	.75±.1	1.48±.28	.93±.11	9-38
M3a	41	50	11	1	.94±.07	-.25±.22	.83±.03	1.58±.03	.94±.14	.006-1.1
M3b	11	50	11	4	3.9±.3	-.03±.14	.81±.06	1.55±.1	.88±.17	.8-8.6
M4a	15	100	8	2.9	2.8±.24	-.04±.08	.84±.03	1.57±.03	.9±.1	.004-5.
M4b	41	100	4	1	.88±.09	-.6±.4	.80±.06	1.61±.05	.85±.14	.25-3.3

<sup>a</sup>This run has  $M_9 = 0.2$ .

<sup>b</sup>The intensities have been multiplied by equation (13).